Supporting Information

Operando Evidence for a Universal Oxygen Evolution Mechanism on Thermal and Electrochemical Iridium Oxides

Viktoriia A. Saveleva[a], Li Wang[b], Detre Teschner[c,d], Travis Jones[c], Aldo S. Gago[b], K. Andreas Friedrich[b,e], Spyridon Zafeiratos[a], Robert Schlögl[c,d], Elena R. Savinova[a,**]*

[a]Institut de Chimie et Procédés pour l'Energie, l'Environnement et la Santé, UMR 7515 du CNRS-UdS 25 Rue Becquerel, 67087 Strasbourg, France

[b]Institute of Engineering Thermodynamics, German Aerospace Center (DLR), Pfaffenwaldring 38-40, 70569 Stuttgart, Germany

[c]Departement of Inorganic Chemistry, Fritz-Haber-Institut der Max-Planck-GesellschaftFaradayweg 4–6, 14195 Berlin, Germany

[d]Department of Heterogeneous Reactions, Max-Planck-Institut für Chemische Energiekonversion, Stiftstr. 34-36, 45470, Mülheim a. d. Ruhr, Germany

[e]Institute of Energy Storage, University of Stuttgart, Pfaffenwaldring 31, 70569 Stuttgart, Germany

Corresponding Author

* Current address: Electrochemistry Laboratory, Paul Scherrer Institut, 5232 Villigen, Switzerland

**Corresponding author. Phone: ++33(0)3 68 85 27 39. Fax: ++33(0)3 68 85 27 61.

E-mail: elena.savinova@unistra.fr

1. Materials synthesis and MEA preparation

The catalyst synthesis was performed following procedures reported in previous publications[1–3]. 3.51 g cetyltrimethylammonium bromide (CTAB, Merck Millipore) as capping agent was dissolved in 360 mL anhydrous ethanol (VWR Chemicals), followed by adding 311 mg anhydrous $IrCl_3$ (Alfa Aesar) and dissolving in 150 mL anhydrous ethanol. After keeping the reaction mixture under strong agitation in Ar atmosphere (Linde, 5.0) for 0.5 h, 60 mL anhydrous ethanol containing 456 mg dissolved $NaBH_4$ (VWR Chemicals) was slowly added to the above solution with a flow speed of 12 mL min^{-1}. The reaction lasts 5 hours until the color of the reaction mixture turns to black completely. The reduced metallic Ir nanoparticles were gathered by a centrifuge with a rotating speed of 7600 rpm, then rinsed by a large amount of pure ethanol and deionized water, dried in an oven under air at 40 ^oC overnight. Regarding the thermally synthesized rutile phase IrO_2, the as prepared metallic Ir nanoparticles were further treated in a Muffle furnace at 490 ^oC under atmospheric environment for 0.5 h. The heating ramp used for this process was 5 ^oC min^{-1}.

The MEAs were obtained by the catalyst-coated membrane method using Aquivion ionomer (Solvay). The catalyst inks were prepared by mixing iso-propanol and water (1/1) with the catalyst powder of either metallic iridium or iridium oxide particles for the anode side and Pt/C – for the cathode side, respectively. After spraying the MEAs were hot pressed. The working electrode (WE) side loading was 0.1 mg cm^{-2} , while the counter electrode loading was 10 times higher (metal basis). For further details of the MEA preparation the reader is referred to Saveleva et al.[2]

2. Transmission electron microscopy

Transmission electron microscopy was used to characterize the catalysts before the MEA fabrication as well as post-mortem by scraping the catalyst particles from the WE surface of the MEAs. Scanning transmission electron microscopy (STEM) was performed with a LaB6-JEOL 2100 microscope operating at 200 kV with a point to point resolution of 0.1 nm. Typical STEM images of electrocatalyst powders before and after NAP-XPS measurements are shown in **Figure S 1**. Comparison of STEM images of Ir nanoparticles before and after the NAP-XPS measurements (Ir@IrO_x sample) shown in Panels A and B of **Figure S 1**, correspondingly, revealed a slight growth of the mean particle size during the operation from ca. 2.0 nm for the pristine metallic powder to ca. 2.4 nm for Ir@IrO_x catalyst after the spectroelectrochemical measurements. In both cases, the particles are highly agglomerated. Panels C and D demonstrate the rod-like shape of IrO_2 particles. The mean width was equal to ca. 5.5 nm and the length to ca. 15.0 nm while no changes either in the particles size or in their shape were detected in the post-mortem sample.

The specific surface area was roughly estimated from the mean particle size defined from the microscopic images. Neglecting the agglomeration of the particles observed both for the electrochemical and thermal oxide, the resulting values were ca. 130 and 74 m^2g^{-1} for Ir@IrO_x and IrO_2, correspondingly.

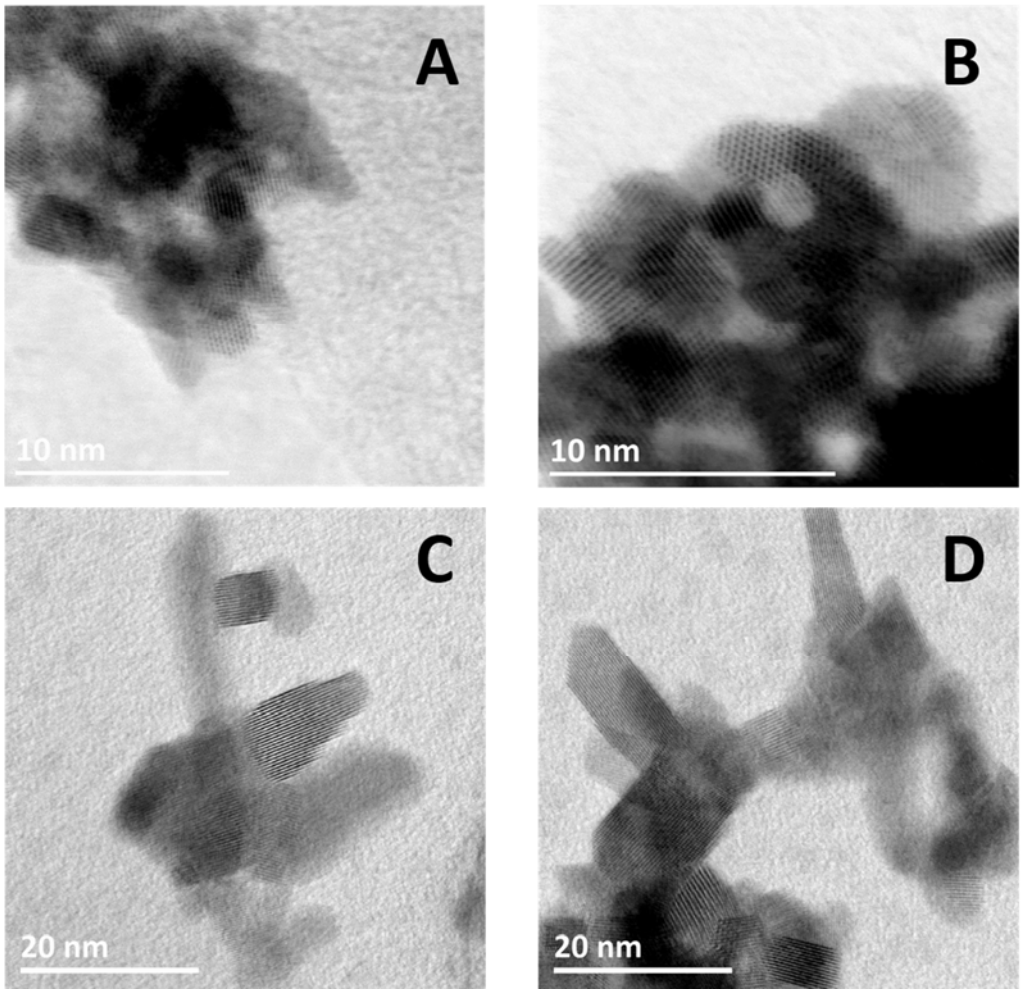

Figure S 1. STEM images of Ir@IrO_x (A, B) and IrO_2 (C, D) catalysts before (A,C) and after (B, D) operando spectroelectrochemical measurements.

3. X-ray powder diffraction (XRD)

XRD analysis of the catalyst powders (metallic Ir and thermal oxide IrO_2) was performed using Bruker D8 Advance diffractometer with a Cu source. Both diffractograms as well as the characteristic reflexions of the reference compounds (stars) are shown in **Figure S 2**. The latter were taken from the database of the International Centre for Diffraction Data (ICDD). For metallic Ir powder we observed wide reflexes attributed to nanoparticles of metallic Ir but also the traces of not-reacted salt ($IrCl_3$). The contribution of the $IrCl_3$ being small, its observation in the powder diffraction patterns can be attributed to the large size of $IrCl_3$ crystals (see Ref.[9]). IrO_2 sample is fully represented by the rutile phase oxide.

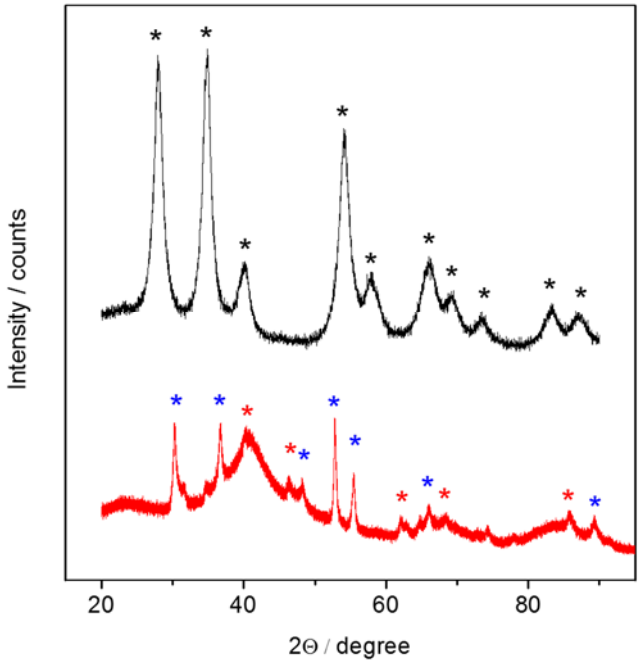

Figure S 2. XRD patterns of catalysts powders: metallic Ir (red), thermal oxide IrO_2 (black). The ICDD data for rutile IrO_2 (black, 01-088-0288), face-centered cubic Ir (red, 00-046-1044), $IrCl_3$ (blue, 01-073-0745) are marked in the diffraction pattern.

4. Electrochemical characterization in liquid electrolyte and under water vapor ambient

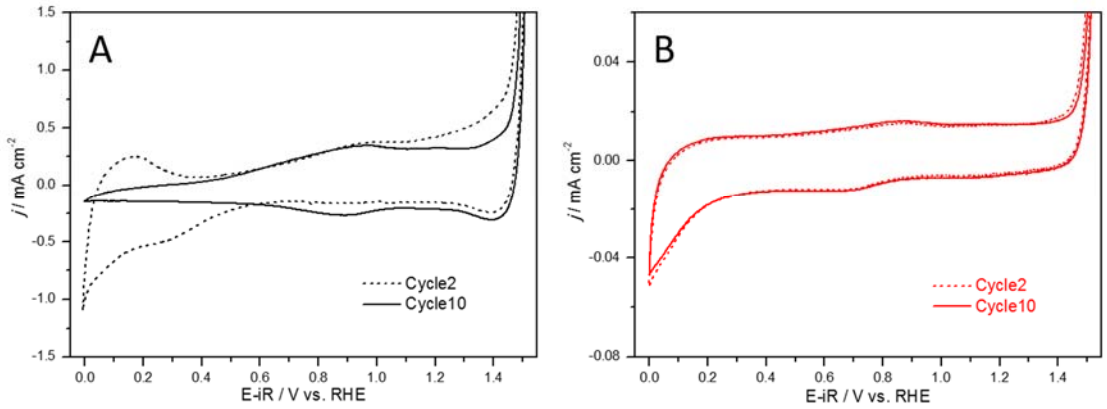

Figure S 3. Cyclic voltammograms obtained in N_2-saturated 0.05 M H_2SO_4 on Ir@IrO_x anode (A) and IrO_2 (B) at the sweep rate of 20 mV s^{-1} at 25 °C. Catalyst loading on the GC surface is 60 µg cm^{-2}. Current density is normalized to the geometric surface area of the electrode.

For both Ir@IrO_x and IrO_2 electrodes, 10 cycles of cyclic voltammetry (CV) were applied before the oxygen evolution reaction (OER) evaluation. The 2nd and the 10th cycle for Ir@IrO_x are presented in Panel A of Figure S 3, the disappearance of the hydrogen adsorption/desorption peaks in low potential range (0 V – 0.5 V *vs.* RHE) after 10 cycles of CV clearly indicate the formation of electrochemically oxidized IrO_x on the particle surface. The corresponding curves for IrO_2 are shown in Panel B of Figure S 3 for comparison. No apparent changes are observed after subsequent potential cycles, implying that the rutile phase IrO_2 is electrochemically stable and no significant changes occur on the electrode surface during the potential cycling.

Figure S 4 shows typical CVs recorded on Ir@IrO_x – based and IrO_2 – based MEAs in the NAP-XPS chamber under 3 mbar water vapor. The curve recorded on Ir@IrO_x demonstrates two red-ox peaks with anodic peak potentials around 0.5 V and 1.2 V vs DHE, while the CV obtained on thermal iridium oxide – at 0.5 V and 1.0 V vs DHE. The shift of the peaks observed under water vapor conditions in comparison to 0.05 M H_2SO_4 for both catalysts is probably related to a lower water activity and the absence of mobile anions.

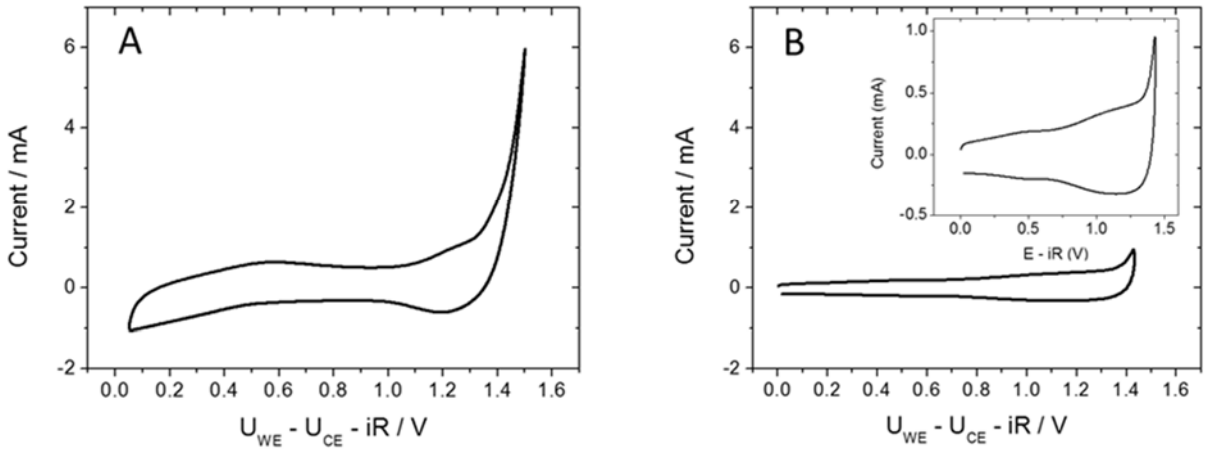

Figure S 4. Cyclic voltammograms obtained in the NAP-XPS chamber under 3 mbar water vapor on Ir@IrO$_x$ (A) and IrO$_2$ (B) anodes. The inset of Panel B represents a magnified voltammogram of the IrO$_2$ anode. Scan rate 50 mV s^{-1}.

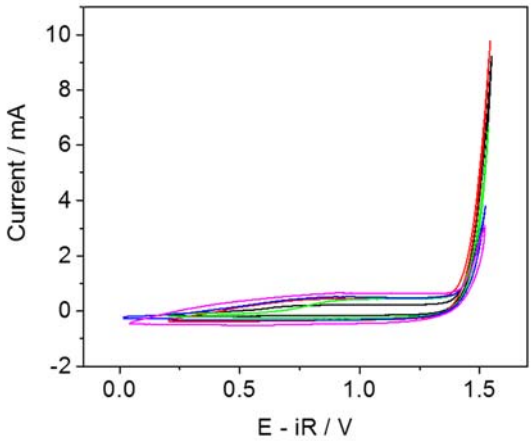

Figure S 5 shows the effect of relative humidity on the CV recorded on Ir@IrO$_x$ anode. The analysis of the Tafel slope in the OER interval did not reveal significant differences depending on the water vapor pressure. However, the Tafel slopes are higher than the one, estimated from the voltammograms obtained in liquid 0.05 M H_2SO_4 electrolyte.

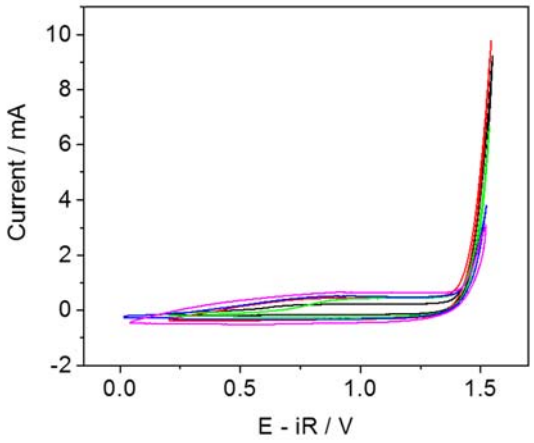

Figure S 5. The cyclic voltammograms recorded on Ir@IrO_x electrode under different water vapor pressures: 23.5 mbar (red), 16 mbar (black), 9 mbar (green), 4.5 mbar (blue), 3 mbar (magenta). Scan rate 5 mV s^{-1}. The catalyst loading was 0.1 mg cm^2.

5. *Operando* spectroscopic measurements

5.1. Measurement protocol

The spectroscopic measurements (NAP-XPS and soft X-rays XANES) were performed at the ISISS beamline (BESSY II synchrotron at the Helmholtz Zentrum Berlin) in a set-up previously described[4,5] under 3 mbar oxygen-free water vapor under constant voltage applied between the working and the counter electrodes. Spectra were acquired after a delay time of 120 s necessary to stabilize the current and thus perform measurements at a constant Ohmic drop-corrected E-iR potential. The electrochemical activity of the MEAs was measured by cyclic voltammetry before the start of the NAP-XPS/XANES measurements and then monitored at the end of the measurement cycle. The current values were followed by means of chronoamperometry. A μ-AutoLab potentiostat from Metrohm was used for the electrochemical studies. The formation of hydrogen on the cathode side of the MEA under the operation conditions allows us to use the counter electrode as a dynamic hydrogen electrode (DHE) as it was previously shown in Ref.[2] The OER onset potential, confirmed by the on-line quadrupole mass spectrometer, corresponds to the values obtained in liquid electrolyte allowing us to use the obtained potential values without correction. The MEA resistance was examined using high frequency impedance spectroscopy measurements throughout the experiment and was used to perform the Ohmic drop (iR) correction. The timeline of the experiments is described in the main text.

The O K edge spectra were recorded under different polarization conditions, Auger (AEY) and total electron yield (TEY) modes were registered simultaneously. The excitation energy was scanned between 523 eV and 550 eV.

The NAP-XPS measurements were performed separately after the adsorption edge studies. Ir4f, C1s and O1s XP spectra were recorded using selected excitation energies so that the photoelectrons were emitted at a kinetic energy of ca. 530 eV. To increase the surface sensitivity Ir4f spectra were also recorded at kinetic energy of 330 eV. These values correspond to an approximate analysis depth (estimated as three times the inelastic mean free path) of 1.7 nm and 2.3 nm for 330 eV and 530 eV respectively. To determine the surface atomic ratios (ARs), the spectral intensities were normalized by the energy dependent incident photon flux. The binding energy (BE) scale was calibrated with respect to the Fermi edge of the electron analyzer.

5.2. O K edge. Fitting and analysis

As it was shown in Pfeifer et al.[6] the low excitation energy region (from 523 to 530 eV) is not affected by the signals from the continuous presence of the gas-phase water and oxygen in the NAP-XPS chamber. After the normalization to the incident photon flux and to the gas-phase peaks intensity the O K edge spectra can be used to determine the surface coverage[7]. To obtain a reliable background containing only water gas-phase peaks we measured the O K edge spectra in the absence of the sample. The obtained curve was used as a background and was subtracted from all the spectra. The example of subtraction is shown in Figure S 6.

Regardless the higher surface sensitivity of AEY in comparison to the TEY, the latter usually provides better signal-to-noise ratios which allowed us to analyze the low intensities of the pre-edge region. The evolution of this region in TEY mode under polarization for Ir@IrO_x and IrO_2 anodes is shown in Figure S 7 and Figure S 8 correspondingly.

The fitting of the O K edges recorded on IrO_2 electrode was done based on the parameters reported in the work of Pfeifer et al.[8] where the position and the shape of the peaks corresponding to the O^{I-} and O^{II-} species were defined on the basis of the corresponding density functional theory calculations. The additional peak at 529.6 eV observed on Ir@IrO_x sample was attributed to μ_1-OH species as it was explained in the main text. The potential dependence of this peak intensity with applied potential is shown in Figure S 9. The fitting of the peaks was done with Gaussian/Lorentzian GL(30) function of constant width. Taking into account the low intensity of the pre-edge, by varying the fitting parameters we estimated the error as 10%.

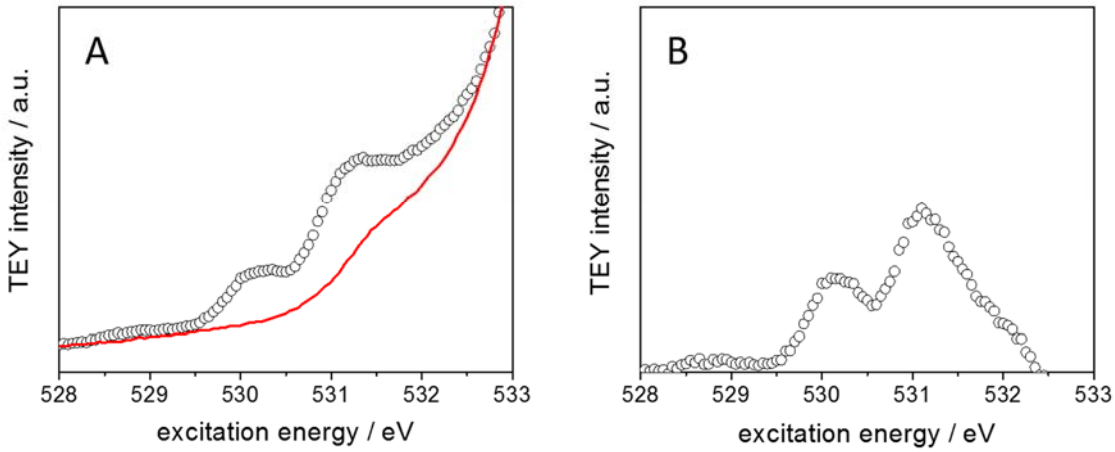

Figure S 6. Low excitation energy of O K edges (TEY) of IrO_2 anode under 3 mbar water vapor and 1.53 V before (A) and after (B) background subtraction. The background is marked red in Panel A.

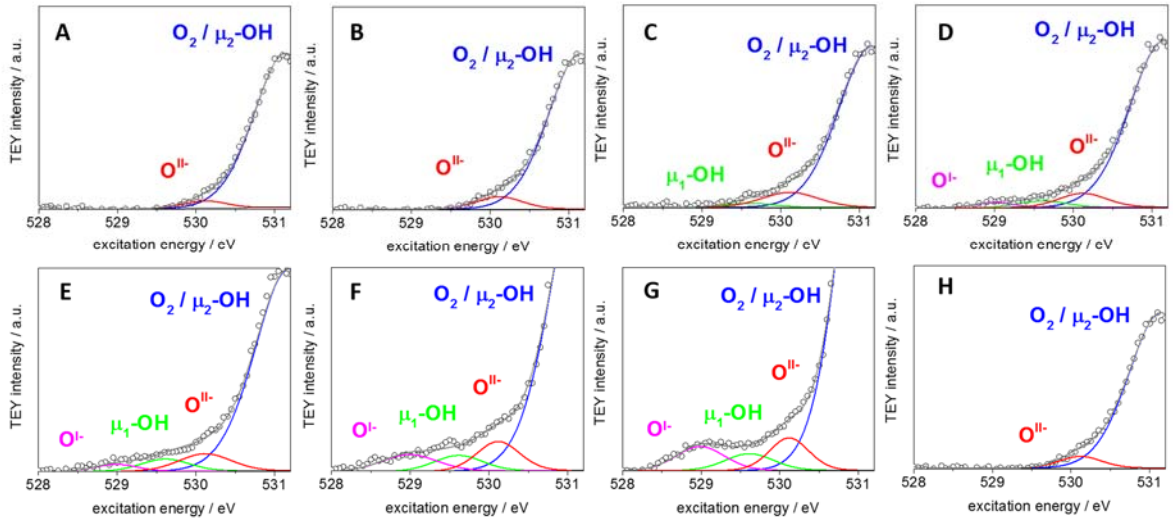

Figure S 7. Low excitation energy of O K edges (TEY) of Ir@IrOx anode under 3 mbar water vapor and different polarization conditions (E-iR): 0 V (A); 1.0 V (B); 1.1 V (C); 1.29 V (D); 1.38 V (E); 1.43 V (F); 1.48 V (G); 0 V backward (H). Color code: O^{I-} (magenta), O^{II-} (red), gas-phase O_2 / μ_2 – OH (blue), μ_1 – OH (green) experimental data (black circles), fitted spectrum (grey).

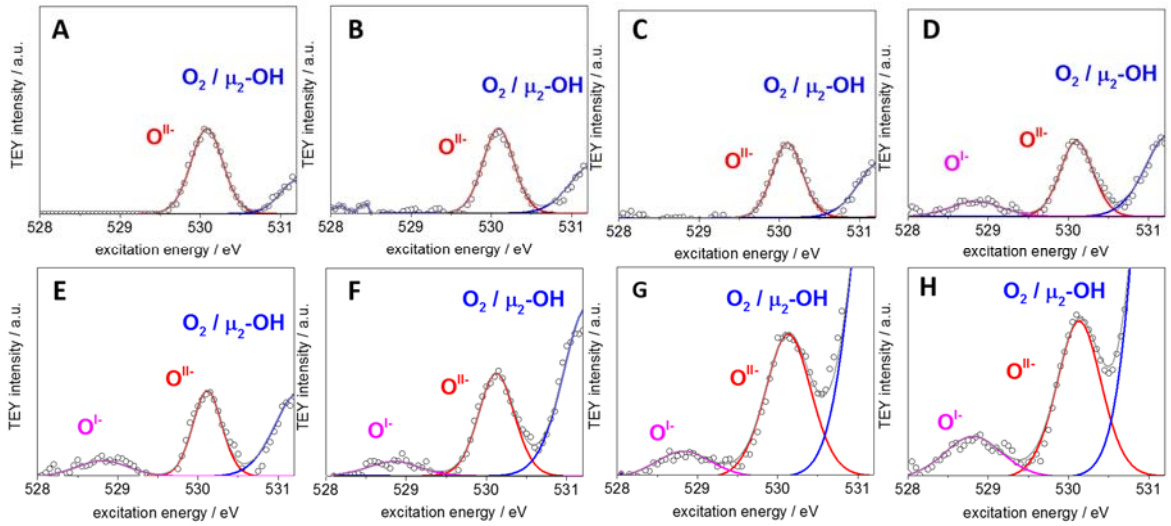

Figure S 8. Low excitation energy of O K edges (TEY) of IrO_2 anode under 3 mbar water vapor and different polarization conditions (E-iR): 0 V (A); 0.25 V (B); 0.7 V (C); 1.3 V (D); 1.4 V (E); 1.47 V (F); 1.53 V (G): 1.56 V (H). Color code: O^{I-} (magenta), O^{II-} (red), gas-phase O_2 / μ_2 – OH (blue), experimental data (black circles), fitted spectrum (grey).

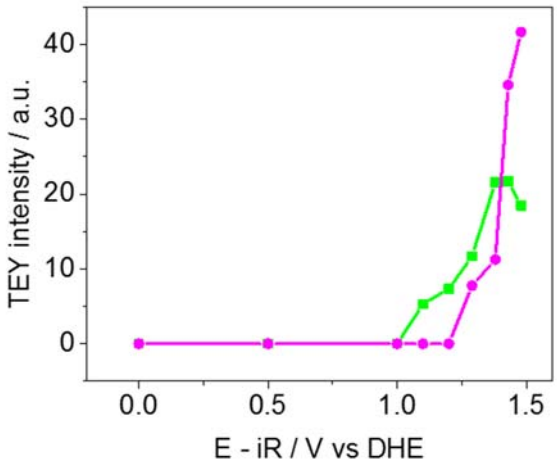

Figure S 9. TEY intensity of μ_1 – OH (green) and O^{I-} (magenta) peaks observed on O K edge spectra (see Figure S 7) recorded for Ir@IrO_x anode versus Ohmic drop-corrected potential.

5.3. O1s XP spectra analysis

Figure S 10 shows O1s XP spectra on the two anodes acquired at the end of the experiment. Compared to the spectrum of the Ir@IrO_x anode obtained before the measurements (see Figure 2 of the main text), one may see the increase of the low BE component in panel A at 530 eV, which may be attributed to the ageing of the electrochemical oxide accompanied by an increase in the contribution of lattice oxygen after the two OER cycles (recording of O K edge and Ir4f spectra) also observed in the O K edge spectra (see Figure S 7).

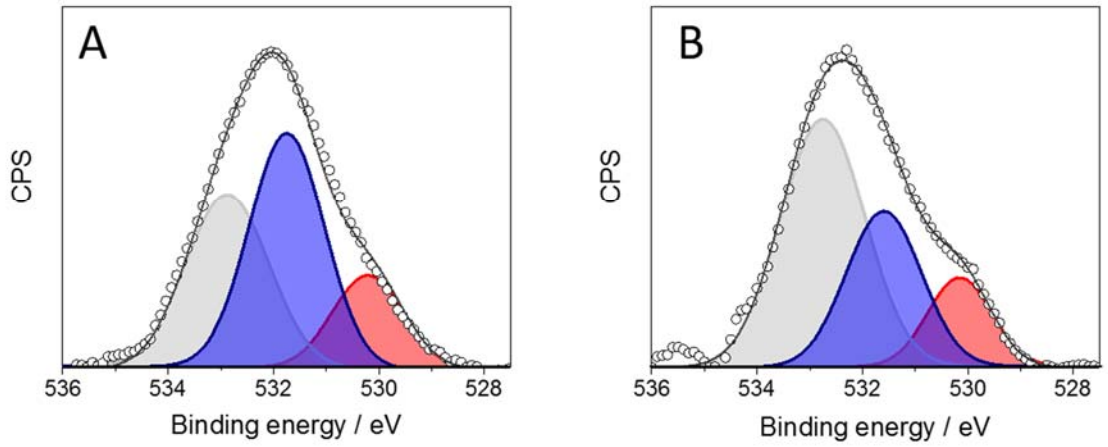

Figure S 10. O1s XP spectra of Ir@IrO_x (A) and IrO_2 (B) anodes under 3 mbar water vapor and OER conditions (E – iR = 1.48 V) obtained after two full OER cycles. Fitting: lattice oxide – red, hydroxide and C=O species - blue, water and C - O species – grey. Kinetic energy: 530 eV. Background subtraction was carried out using Shirley method and curve fitting was performed based on a Gaussian/Lorentzian GL(30) function.

5.4. Ir4f XP spectra: evolution under potential. Quantitative analysis

Fitting of the spectra was performed using five doublets with $Ir4f_{7/2}$ peak positions at 60.85 eV, 61.70 eV, 63.00 eV, 62.40 eV and 64.20 eV, and attributed to metallic Ir; Ir (IV) and its satellite; Ir (III) and its satellite, correspondingly as it was discussed in our previous publications[2,9]. Ir4f XP spectra recorded on Ir@IrO_x anode under different polarizations and 2 photon energies are displayed in Figure S 11 and Figure S 12. One may clearly see the decreasing of Ir (III) component contribution and the growth of Ir (IV) with potential. The backward scan is represented by two potentials E = 1.1 V and 0 V shown in the panels H and I of Figure S 11, respectively. The observed gradual increasing of Ir (III) corresponds to the transition Ir (IV) / Ir (III) observed also in the CVs (***Figure S 4***). The quantitative analysis of Ir components versus potential is shown in Figure 4 of the main text.

Figure S 13 demonstrates the Ir4f XP spectra recorded at kinetic energy of 330 eV on IrO_2 sample, the difference spectra are presented at the top of the plot.

Figure S 14 shows the Ir4f spectra of two reference samples: IrO_2 and $IrO_2 \cdot 2H_2O$ (Aldrich) fitted with the parameters used above. The analysis revealed the presence of Ir (III) component in

hydrated oxide (ca. 25%). The shape of the Ir4f spectra measured for the reference rutile oxide (commercial) is identical with the one obtained for the IrO_2 anode.

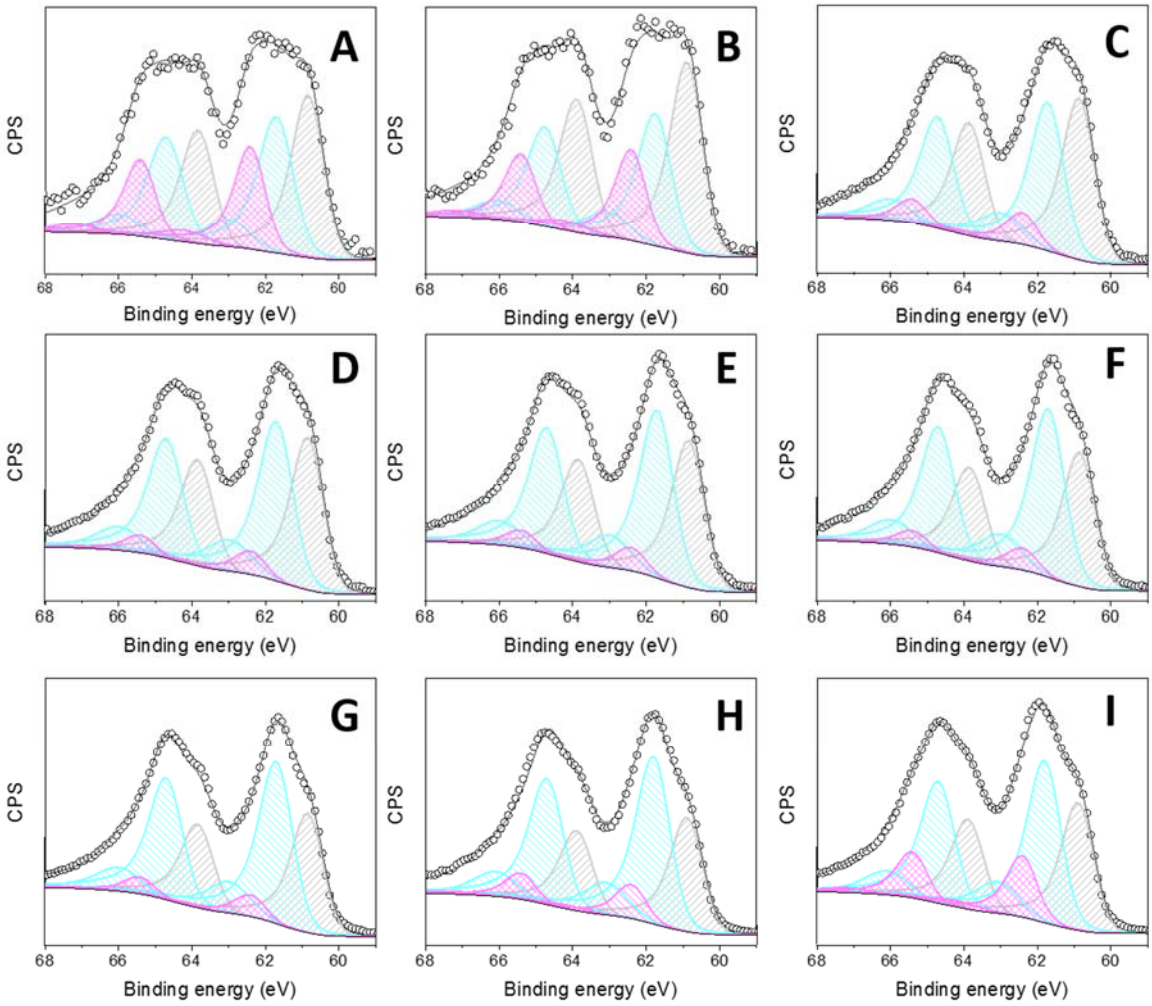

Figure S 11. Ir4f XP spectra of Ir@IrO_x anode under 3 mbar water vapor and different polarization conditions (E-iR): A – 0 V; B – 0.3 V; C – 1.1 V; D – 1.29 V; E – 1.38 V; F – 1.43 V; G – 1.48 V; H – 1.1 V (backward scan); I – 0 V (backward scan). Color code: Ir (met) – grey, Ir (III) magenta, Ir (IV) – cyan. Kinetic energy 530 eV.

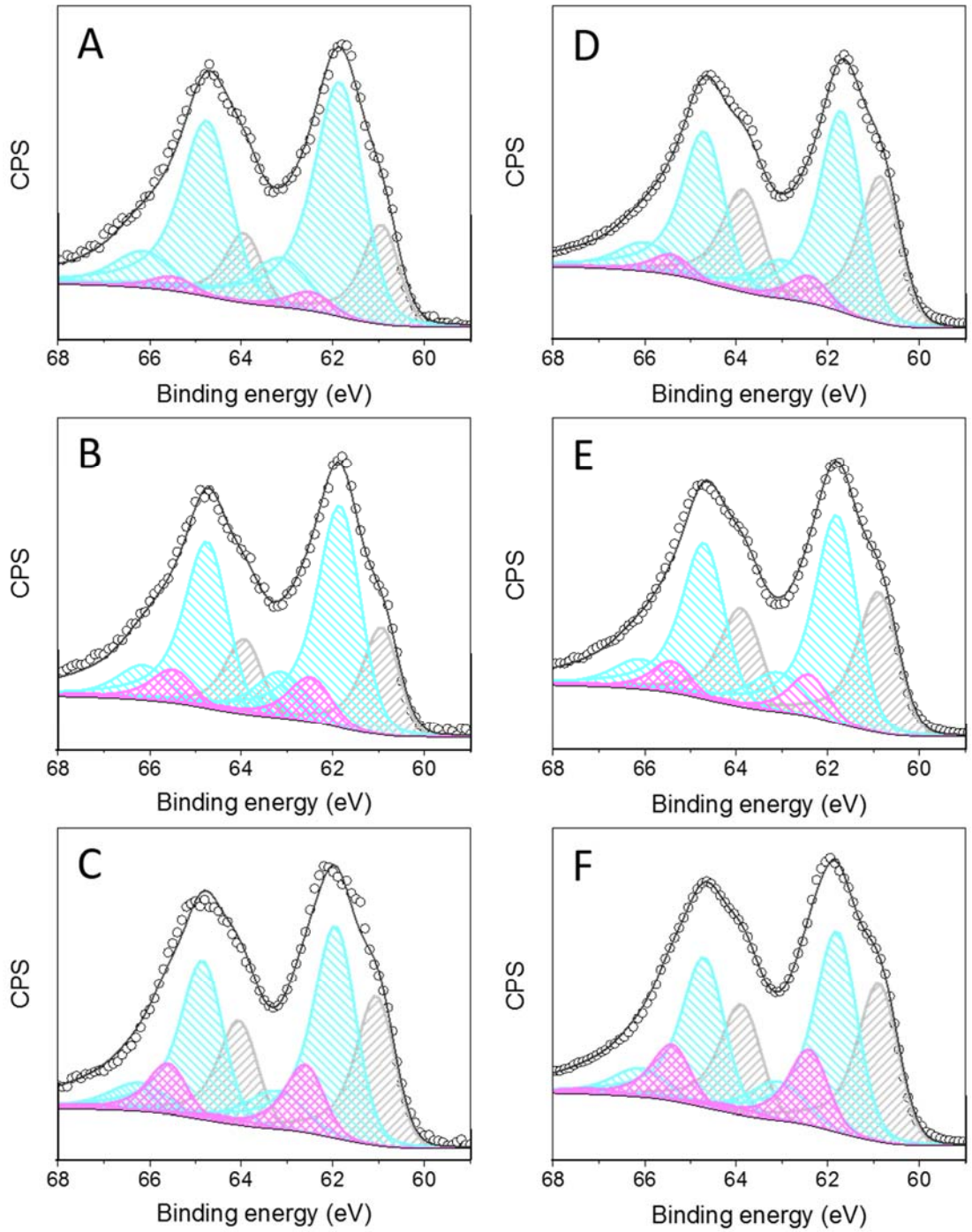

Figure S 12. Comparison of Ir4f XP spectra of Ir@IrO_x anode acquired at different kinetic energy of photoelectrons: 330 eV (A-C) and 530 eV (D-F) under 3 mbar water vapor and different polarization conditions (E-iR): A, D – 1.48 V; B, E – 1.1 V (backward scan); C, F – 0 V (backward scan). Fitting: Ir (met) – grey, Ir (III) – magenta, Ir (IV) – cyan.

Table 1. Contributions of various components to the Ir4f spectra for different kinetic energies of photoelectrons (330 and 530 eV)

	530 eV			330 eV		
Component, %	**1.5 V**	**1.1 V back**	**0 V back**	**1.5 V**	**1.1 V back**	**0 V back**
Ir met	30,4	28,5	29,2	17,2	18,5	26,8
Ir IV	61,6	60,9	53,6	76,3	70,1	57,5
Ir III	8,0	10,6	17,2	6,5	11,4	15,7

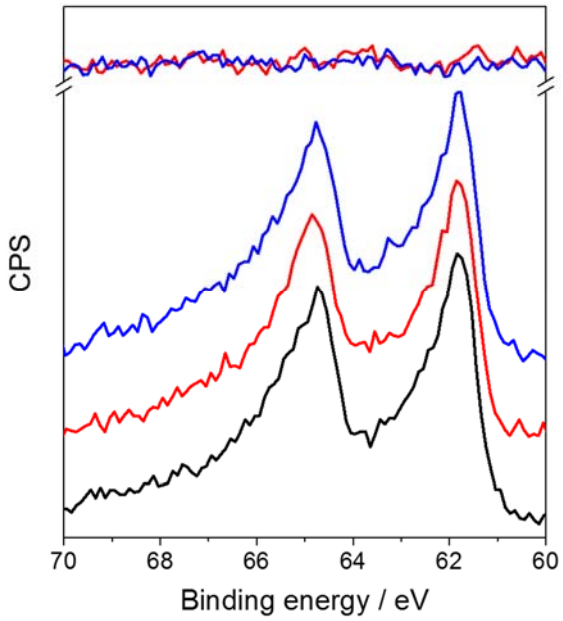

Figure S 13. Ir4f XP spectra of IrO_2 anode under 3 mbar water vapor and different polarization conditions (E-iR): 0 V (black); 1.3 V (red); 1.58 V (blue). The upper part of the figure represents the difference between the spectra obtained under the open circuit condition and higher anodic potentials. Kinetic energy: 330 eV.

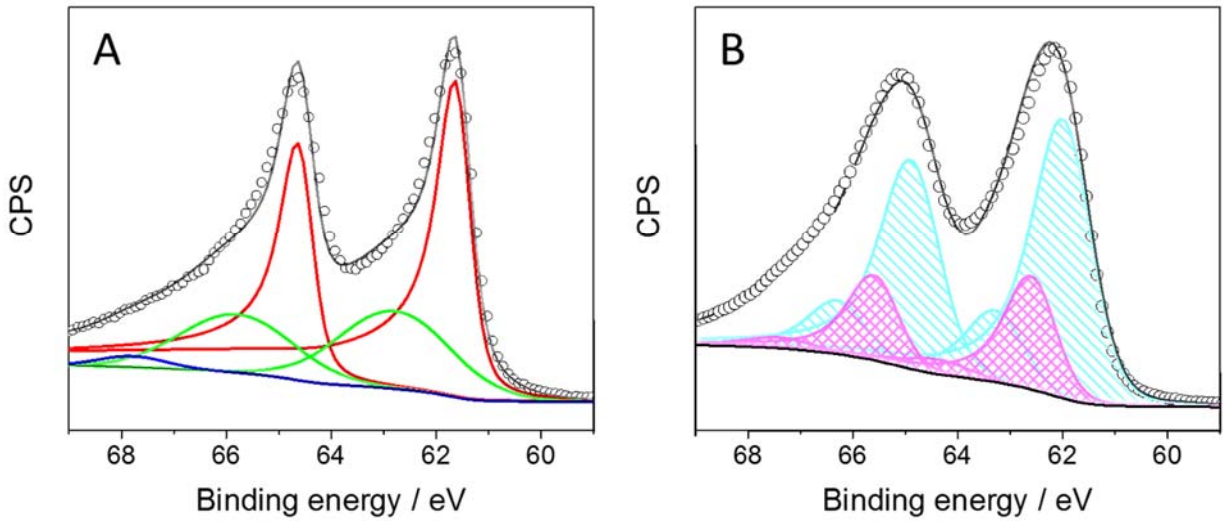

Figure S 14. Ir4f XP spectra recorded under UHV on commercial samples (Alfa Aesar): IrO_2 (Panel A) and $IrO_2 \cdot 2H_2O$ (Panel B). Color codes for Panel A: Ir (IV) - red; Ir (IV) sat 1 - green; Ir (IV) sat 2 – blue. Color codes for Panel B: Ir (IV) and its satellite - cyan; Ir (III) and its satellite - magenta. Photon energy 595 eV.

6. DFT calculations

Density functional theory (DFT) calculations were performed using the Quantum ESPRESSO package version 6.1.[10] To recover the correct ground state properties[11] the Perdew, Burke, and Ernzerhof (PBE) exchange and correlation potential was employed[12]. Projector augmented wave datasets were taken from the PS Library[13] and a kinetic energy (charge density) cutoff of 30 Ry (300 Ry) was employed. A **k**-point mesh equivalent to at least (8×8) for the (1×1) (001) surface unit cell was employed with cold smearing[14] using a smearing parameter of 0.02 Ry. Calculations used at least 5 layers of IrO_2, the central two layers were fixed and the other were allowed to relax. Various surface terminations [(110), (200), (201), (210), (111)] were investigated with O and OH terminations. The role of Ir defects introduced at the surface was also tested. Oxygen K-edge spectra were computed using a one-electron Fermi's golden rule expression as implemented in XSpectra.[15,16] These were performed with the same **k**-point mesh as the ground state calculation and no core hole potential was included as this has been shown to give the correct results for rutile-type and defective IrO_2.[17] The relative edge positions were computed by way of a ΔSCF calculation.[18] These relative energies were then aligned using a calculation of bulk IrO_2, under the assumption that the O 1s binding energy of lattice oxygen is 530.0 eV. The potential at which O^{I-} forms was computed using the concept of a theoretical hydrogen electrode,[19] where the reaction energy for hydrogen removal from the surface is calculated by way of DFT. This energy is then corrected for the electrode potential and changes in entropy. We neglected changes in zero point energy as previous investigations show they only contribute 0.1-0.2 eV for the types of species we are concerned with and will therefore not qualitatively change our findings.

To sample a sufficient large number of possible local surface structures DFT calculations were performed on fully-oxidized pristine rutile-type IrO_2 surfaces with (110), (100), (201), (210), and (111) surface terminations, see Figure S 15. Each of these surfaces display μ_1-O and μ_2-O terminal oxygen ligands. In total we examined 9 μ_1-O and 5 μ_2-O in this way.

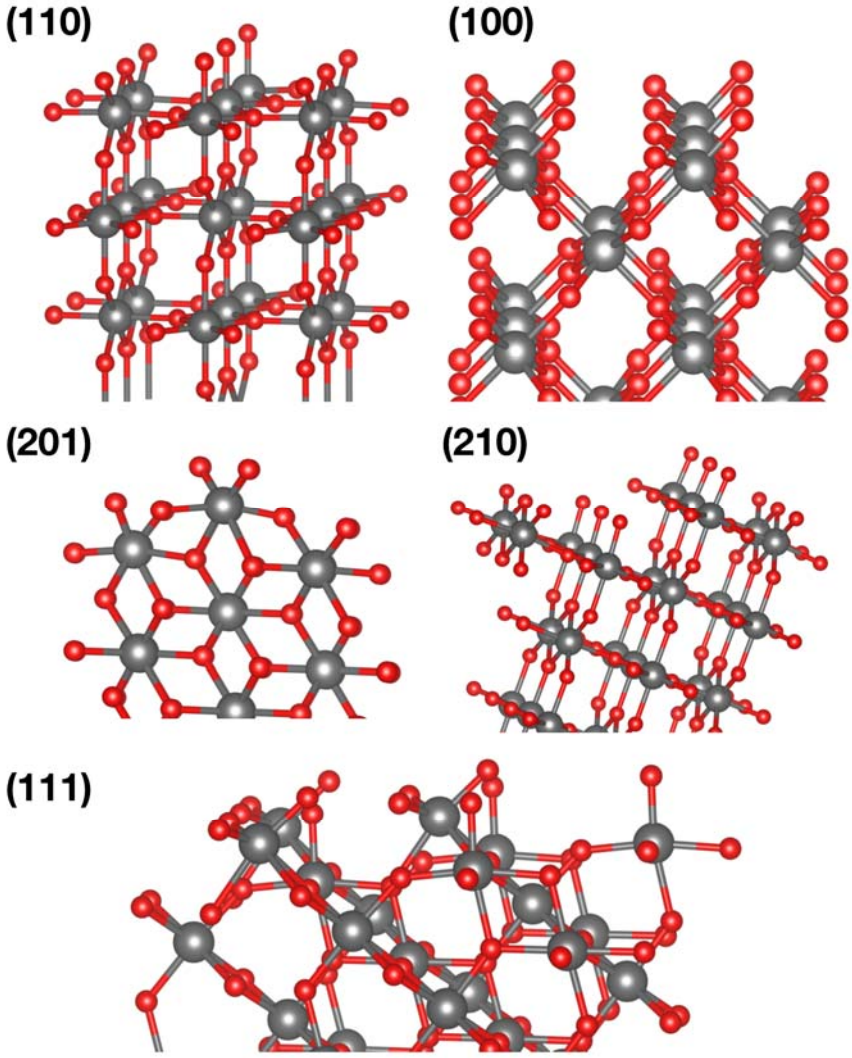

Figure S 15. Pristine surface terminations used to compute the O K-edge spectra and Löwin charges on μ_1-O and μ_2-O species.

We also computed the O K-edges of these surfaces with a variety of Ir surface vacancies. On the (110), for instance, we examined the two types of surface vacancy shown in Figure S 16, where the missing Ir atom is shaded white for clarity. In the case of the structure labeled (110) Ir_{br} vacancy a surface Ir atom involved in Ir-O-Ir bridging bonds on the surface has been removed. In this case the surface O:Ir ratio increases because only an iridium atom is removed. For the Ir_{cus} vacancy a coordinatively unsaturated Ir has been removed from the surface, which also requires the removal of O bound to the CUS site, as such, the O:Ir ratio remains fixed. Such calculations were performed for the (110), (201), (210), yielding 24 distinct μ_1-O geometries and 11 different μ_2-O geometries.

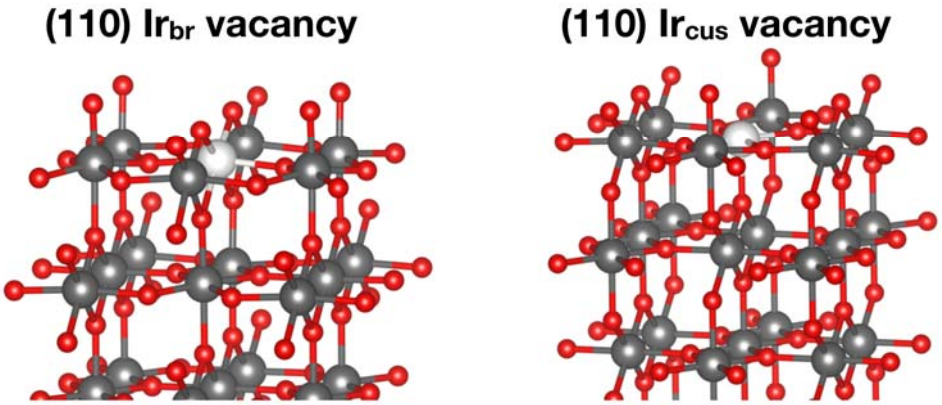

Figure S 16. Defective (110) surface terminations used to compute the O K-edge spectra and Löwin charges on μ_1-O and μ_2-O species. The white atom indicates the position of the vacancy.

OH terminated surfaces were also investigated. For this purpose we examined the fully hydrogenated pristine (110), (200), (201), and (210) surfaces. The (200), (201), and (210) surfaces are shown in Figure S 17. This procedure resulted in 10 distinct μ_1-OH and 2 μ_2-O geometries, which allowed us to investigate the role of hydrogen bonding on the white line position in the O K-edge and the Löwdin charge.

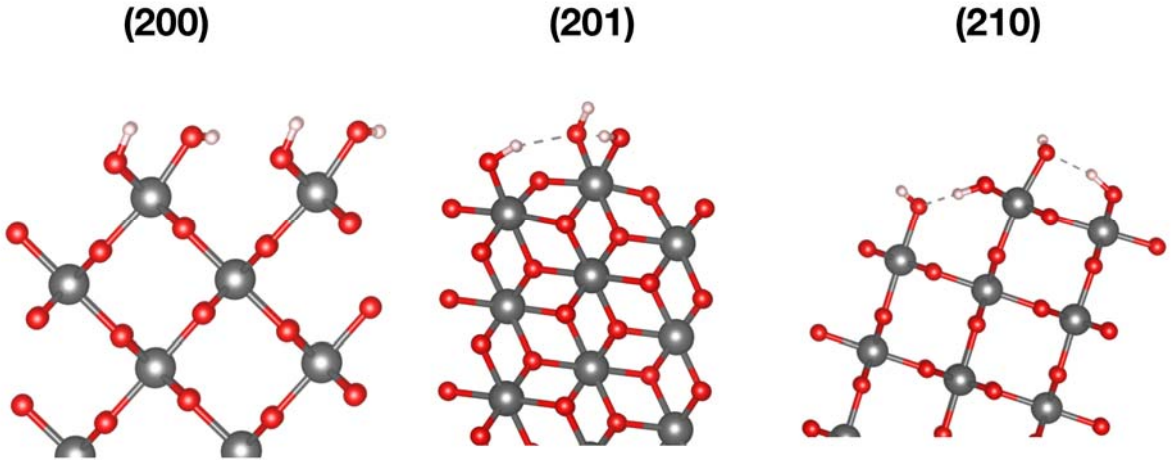

Figure S 17. (200), (201), and (210) OH terminated surfaces used to compute the O K-edge spectra and Löwdin charges on μ_1-OH and μ_2-OH species.

References

(1) Lettenmeier, P.; Wang, L.; Golla-Schindler, U.; Gazdzicki, P.; Cañas, N. A.; Handl, M.; Hiesgen, R.; Hosseiny, S. S. S.; Gago, A. S.; Friedrich, A. K. Nanosized IrOx-Ir Catalyst with Relevant Activity for Anodes of PEM Electrolysis Produced by a Cost-Effective Procedure. *Angew. Chemie* **2015**, *128*, 752–756.

(2) Saveleva, V. A.; Wang, L.; Luo, W.; Zafeiratos, S.; Ulhaq-Bouillet, C.; Gago, A. S.; Friedrich, K. A.; Savinova, E. R. Uncovering the Stabilization Mechanism in Bimetallic Ruthenium–Iridium Anodes for Proton Exchange Membrane Electrolyzers. *J. Phys. Chem. Lett.* **2016**, *7*, 3240–3245.

(3) Wang, L.; Saveleva, V. A.; Zafeiratos, S.; Savinova, E. R.; Lettenmeier, P.; Gazdzicki, P.; Gago, A. S.; Friedrich, K. A. Highly Active Anode Electrocatalysts Derived from Electrochemical Leaching of Ru from Metallic Ir 0 .7 Ru 0 .3 for Proton Exchange Membrane Electrolyzers. *Nano Energy* **2017**, *34*, 385–391.

(4) Salmeron, M.; Schlögl, R. Ambient Pressure Photoelectron Spectroscopy: A New Tool for Surface Science and Nanotechnology. *Surf. Sci. Rep.* **2008**, *63* (4), 169–199.

(5) Knop-Gericke, A.; Kleimenov, E.; Hävecker, M.; Blume, R.; Teschner, D.; Zafeiratos, S.; Schlögl, R.; Bukhtiyarov, V. I.; Kaichev, V. V.; Prosvirin, I. P.; et al. Chapter 4 X-Ray Photoelectron Spectroscopy for Investigation of Heterogeneous Catalytic Processes. *Adv. Catal.* **2009**, *52*, 213–272.

(6) Pfeifer, V.; Jones, T. E.; Velasco Vélez, J. J.; Arrigo, R.; Piccinin, S.; Hävecker, M.; Knop-Gericke, A.; Schlögl, R. In Situ Observation of Reactive Oxygen Species Forming on Oxygen-Evolving Iridium Surfaces. *Chem. Sci.* **2017**, *8*, 2143–2149.

(7) Stöhr, J. *NEXAFS Spectroscopy*; Springer-Verlag Berlin Heidelberg, **1992**.

(8) Pfeifer, V.; Jones, T. E.; Velasco Vélez, J. J.; Massué, C.; Greiner, M. T.; Arrigo, R.; Teschner, D.; Girgsdies, F.; Scherzer, M.; Allan, J.; et al. The Electronic Structure of Iridium Oxide Electrodes Active in Water Splitting. *Phys. Chem. Chem. Phys.* **2016**, *18*, 2292–2296.

(9) Lettenmeier, P.; Majchel, J.; Wang, L.; Saveleva, V. A.; Zafeiratos, S.; Savinov, E. R.; Gallet, J. J.; Bournel, F.; Gago, A. S.; Friedrich, K. A. Highly Active Nano-Sized Iridium Catalysts: Synthesis and Operando Spectroscopy in Proton Exchange Membrane Electrolyzer. Chem. Sci., **2018**, *9*, 3570-3579.

(10) Giannozzi, P.; Baroni, S.; Bonini, N.; Calandra, M.; Car, R.; Cavazzoni, C.; Ceresoli, D.; Chiarotti, G. L.; Cococcioni, M.; Dabo, I.; et al. QUANTUM ESPRESSO : A Modular and Open-Source Software Project for Quantum Simulations of Materials. *J Phys. Condens Matter* **2009**, *21*, 395502–395521.

(11) Ping, Y.; Galli, G.; Goddard, W. A. I. Electronic Structure of IrO2 : The Role of the Metal D Orbitals. *J Phys Chem C* **2015**, *119*, 11570–11577.

(12) Perdew, J. P.; Burke, K.; Ernzerhof, M. Generalized Gradient Approximation Made Simple. *Phys. Rev. Lett.* **1996**, *77* (18), 3865–3869.

(13) Corso, A. D. Pseudopotentials Periodic Table : From H to Pu. *Comput. Mater. Sci.* **2014**, *95*, 337–350

(14) Marzari, N.; Vanderbilt, D.; Vita, A. De; Payne, M. C. Thermal Contraction and Disordering of the Al (110) Surface. *Phys. Rev. Lett*. **1999**, 82 (16), 3296–3300.

(15) Gougoussis, C.; Calandra, M.; Seitsonen, A. P.; Mauri, F. First-Principles Calculations of X-Ray Absorption in a Scheme Based on Ultrasoft Pseudopotentials: From α-Quartz to High-Tc Compounds. *Phys. Rev. B* **2009**, 80, 075102–075110

(16) Taillefumier, M.; Cabaret, D.; Flank, A.; Mauri, F. X-Ray Absorption near-Edge Structure Calculations with the Pseudopotentials: Application to the K Edge in Diamond and Alpha -Quartz. *Phys. Rev. B* **2002**, 66, 195107–195115

(17) Pfeifer, V.; Jones, T. E.; Velasco Vélez, J. J.; Massué, C.; Greiner, M. T.; Arrigo, R.; Teschner, D.; Girgsdies, F.; Scherzer, M.; Allan, J.; et al. The Electronic Structure of Iridium Oxide Electrodes Active in Water Splitting. *Phys. Chem. Chem. Phys*. **2016**, 18, 2292–2296.

(18) Pehlke, E.; Schefiier, M. Evidence for Site-Sensitive Screening of Core Holes at the Si and Ge (001) *Surface. Phys. Rev. Lett*. **1993**, 71 (14), 2338–2341

(19) Rossmeisl, J.; Qu, Z. W.; Zhu, H.; Kroes, G. J.; Nørskov, J. K. Electrolysis of Water on Oxide Surfaces. *J. Electroanal. Chem*. **2007**, 607 (1–2), 83–89.